Climate Dynamics (2025) 63:5
https://doi.org/10.1007/s00382-024-07496-5

ORIGINAL ARTICLE

Cross-equatorial extension of the Pacific-South American wave train enabled by Southeastern South American rainfall

Siyu Zhao[1] · Rong Fu[1] · Sen Zhao[2] · Fei-Fei Jin[2,3] · Hui Wang[4]

Received: 21 July 2024 / Accepted: 28 October 2024

Abstract
The Pacific–South American (PSA) pattern is a key mode of climate variability in the mid-to-high latitudes of the Southern Hemisphere, impacting circulation and rainfall anomalies over South America. However, the effect of South American rainfall on the PSA has not been previously explored. This study focuses on the impact of rainfall over southeastern South American (SESA) during the austral summer (December–February). Observational analyses reveal that the PSA pattern remains confined to higher southern latitudes when SESA rainfall anomalies are weak. In contrast, strong SESA rainfall anomalies can generate a quasi-stationary Rossby wave train, which represents a cross-equatorial extension of the PSA. This wave train propagates along a southwest–northeast great circle path from higher latitudes, crosses the equator, and reaches the tropical Atlantic, southern Europe, and northern Africa, inducing a wet and cool weather condition over western and southern Europe. The observed wave train can be reproduced by the linear baroclinic model (LBM) simulations. Given the PSA's connection to tropical forcing over the central Pacific, we examine differences in the wave response to central Pacific forcing alone versus combined central Pacific and SESA forcings. By incorporating SESA forcing, the wave train originally triggered by central Pacific forcing is amplified and extended. Our findings confirm the significant role of SESA rainfall anomalies in extending the PSA pattern to the Northern Hemisphere and highlight the South American continent as a land bridge that links circulation anomalies across the Pacific and Atlantic Oceans and the Southern and Northern Hemispheres.

Keywords Pacific–South American pattern · Southeastern South American Rainfall · Cross-equatorial waves · Interhemispheric teleconnection · Linear baroclinic model · Diabatic heating

1 Introduction

The El Niño–Southern Oscillation (ENSO) significantly impacts South America, with effects linked to the Walker circulation's descending branch in the tropics (e.g., Kousky et al. 1984; Cai et al. 2020) and Rossby wave trains via the Pacific–South American (PSA) pattern in the extratropics (e.g., Karoly 1989; Mo 2000; Mo and Paegle 2001). The PSA modes are most commonly analyzed using two empirical orthogonal function (EOF) modes, referred to as the PSA-1 and PSA-2, (Mo and Higgins 1998; Mo 2000; Mo and Paegle 2001), though recent studies have introduced new methods for their representation (Irving and Simmonds 2016; Risbey et al. 2021; Goyal et al. 2022; Campitelli et al. 2023). The PSA depicts a zonal wavenumber 3 feature with centers from the central Pacific via the Southern Ocean towards the Atlantic, significantly impacting Southern Hemisphere climate variability (e.g., Mo and Paegle 2001; Müller and Ambrizzi 2007; Irving and Simmonds 2016; Lou et al. 2021; Reboita et al. 2021). Specifically, South American rainfall variability is found to be influenced by Rossby wave trains associated with the PSA (e.g., Mo and Paegle 2001; Hirata and Grimm 2016; Junquas et al. 2016; Gelbrecht et al. 2018; Wang 2019). However, whether such rainfall variability can influence the PSA and extend it to

✉ Siyu Zhao
siyu_zhao@atmos.ucla.edu

1 Department of Atmospheric and Oceanic Sciences, University of California, Los Angeles, Los Angeles, CA, USA

2 Department of Atmospheric Sciences, School of Ocean and Earth Science and Technology (SOEST), University of Hawai'I at Mānoa, Honolulu, HI, USA

3 International Pacific Research Center, SOEST, University of Hawai'I at Mānoa, Honolulu, HI, USA

4 NOAA/NWS/NCEP/Climate Prediction Center, College Park, MD, USA

Published online: 26 November 2024

the Northern Hemisphere has not been investigated previously. Studying the impact of South American rainfall on the PSA can enhance the understanding of teleconnections between the Pacific and Atlantic Oceans and those between the Northern and Southern Hemispheres.

During the austral summer (December–February, DJF), rainfall anomalies over southeastern South America (SESA), the La Plata Basin, are found to be associated with the South American rainfall dipole, which characterizes the intraseasonal rainfall variability of the South American monsoon system (SAMS) (e.g., Boers et al. 2014; Cherchi et al. 2014; Vera et al. 2018; Díaz et al. 2020). Recently, Zhao et al. (2023) demonstrated that SESA rainfall anomalies can induce cross-equatorial propagation of Rossby waves (CEPRW) along a great circle path in the southwest–northeast direction and influence weather patterns over the tropical Atlantic, northwestern Africa and western Europe over a period of 4 days. The influence of SESA rainfall and associated CEPRW are confirmed by equatorward propagating EP-flux anomalies (Edmon et al. 1980) and barotropic model simulations (Ting 1996). The CEPRW arises due to three main factors: (1) the upper-tropospheric westerly wind over tropical regions, which allows Rossby waves to travel between two hemispheres (Dickinson 1968; Webster and Holton 1982; Hsu and Lin 1992; Thomas and Webster 1994), (2) the meridional background flow, locally opening up a tunnel for the one-way propagation of stationary waves across the easterlies (Schneider and Watterson 1984; Li et al. 2015b, 2019; Zhao et al. 2015, 2019), and (3) the diabatic heating associated with convection in the source region, which triggers Rossby wave trains that propagate downstream and potentially cross the equator (Yang and Webster 1990; Ambrizzi and Hoskins 1997; Gong et al. 2020). In particular, diabatic heating is often estimated as the residual of the thermodynamic energy equation, commonly referred to as the apparent heat source Q_1 (e.g., Yanai et al. 1973; Ling and Zhang 2013; Zermeño-Diaz and Zhang 2013; Tseng et al. 2020).

As demonstrated by Mo and Paegle (2001), the relationship between the PSA and South American rainfall has been identified by analyzing cases with extreme PSA amplitudes. For instance, the PSA corresponds to a north–south dipole pattern of rainfall anomalies, with positive rainfall anomalies particularly over the southern part of South America. In our study, we will delve deeper into how positive rainfall anomalies over SESA can, in turn, influence the PSA on intraseasonal time scales. Given that the PSA is generally confined to the mid-to-high latitudes of the Southern Hemisphere, this raises an intriguing question: Can the PSA be extended to the Northern Hemisphere by SESA rainfall through CEPRW?

We will first identify events linked to the daily PSA index, distinguishing those associated with the daily SESA rainfall index from those that are not. This will allow us to categorize events into two groups: those influenced by SESA rainfall and those that are not. Given that the PSA represents the Southern Hemisphere's response to tropical convections such as those linked to the ENSO, Madden–Julian oscillation, and Quasi-biennial Oscillation (Mo and Higgins 1998; Renwick and Revell 1999; Mo and Paegle 2001; Li et al. 2015a), we will use an intermediate atmospheric model, the linear baroclinic model (LBM; Watanabe and Kimoto 2000), to investigate how atmospheric circulation responds to tropical convection alone versus tropical convection combined with SESA rainfall forcing. We will utilize observed heat sources (the diabatic heating) associated with identified events. The LBM, has been successfully used to diagnose wave train pattern response to diabatic heating (e.g., Yasui and Watanabe 2010; Zhao et al. 2015, 2019; Hayashi and Watanabe 2017; Tseng et al. 2019, 2020). In this study, we utilize the LBM because, unlike other complicated atmospheric models, it focuses solely on linear processes and is linearized about observed climatology, eliminating basic state biases. This is crucial, as the Rossby wave pathway is highly dependent on the background flow (Hoskins and Karoly 1981; Hoskins and Ambrizzi 1993; Li et al. 2015b; Zhao et al. 2015), enabling a more accurate representation of atmospheric circulation anomalies in response to diabatic heating.

The rest of the paper is structured as follows. Section 2 describes the data and methodology. Section 3.1 presents the PSA modes and SESA rainfall. Section 3.2 discusses the observational evidence of the extension of the PSA by SESA rainfall. In Sect. 3.3, the LBM simulations are conducted to further confirm the observed findings. Section 4 provides a summary and further discussion of the results.

2 Data and methodology

2.1 Data

The daily precipitation is from National Oceanic and Atmospheric Administration (NOAA) Climate Prediction Center (CPC) Global Unified Gauge-Based Analysis of Daily Precipitation with a spatial resolution of 0.5° (Chen et al. 2008). The daily mean near-surface temperature (2 m), near-surface (10 m) zonal and meridional winds, and multilevel zonal and meridional winds, vertical velocity, air temperature, and geopotential height are from the European Centre for Medium-Range Weather Forecasts fifth-generation reanalysis (ERA5) (Hersbach et al. 2020). The spatial resolution of the near-surface temperature is 1.0° and that of other fields is 2.5°. The analysis period for this study is from 1979 to 2021. Given the focus on the characteristics of composite

events, adding or removing a few years from the dataset will not significantly impact the results.

2.2 Identifying events associated with the PSA and/or SESA rainfall indices

An EOF analysis via a covariance matrix is applied to the monthly 500 hPa geopotential anomalies over the entire Southern Hemisphere with all seasons pooled together following Mo and Paegle (2001). The second (EOF-2) and third EOF (EOF-3) modes represent the PSA-1 and PSA-2, respectively, but these two modes are unable to be separated according to the North test (North et al. 1982). Then, the Kaiser varimax rotation is applied to the EOF modes to obtain rotated EOF (REOF) modes (Richman 1986). The third REOF (REOF-3) mode represents the combined PSA-1 and PSA-2 and will be used in this study. For simplicity, we refer to this combined PSA mode as the PSA. The daily 500 hPa geopotential height anomalies are projected onto REOF-3 to derive the associated principal component (PC) of the PSA. The PC of the PSA is referred to as the PSA index on daily time scales. In addition, daily precipitation anomalies averaged over SESA (20°S–40°S, 50°W–65°W) is referred to as the SESA rainfall index, $[\delta Pr]_{\mathrm{SESA}}$. Both the PSA and SESA rainfall indices are standardized. In this study, we will identify several groups of events with different thresholds of the daily PSA and $[\delta Pr]_{\mathrm{SESA}}$. For each group, when consecutive days satisfy associated requirements, only the first day is used as Day 0 for the composite (e.g., Bowerman et al. 2017). Day −1, Day + 1, …, Day + 5 represents one day before the first day of the composite, one day after the first day of the composite, …, and five days after the first day of the composite, respectively.

2.3 Heating source

We estimate total diabatic heating as the apparent heat source (Q_1) using the approach of Yanai et al. (1973). Following Ling and Zhang (2013), Q_1 is calculated as:

$$Q_1 = \frac{T}{\theta}\left(\frac{\partial\theta}{\partial t} + \vec{V}\cdot\nabla\theta + \omega\frac{\partial\theta}{\partial p}\right), \quad (1)$$

where T, θ, $\vec{V}$, and ω are three-dimensional air temperature, potential temperature, horizonal winds, and vertical velocity, respectively. $\theta = T(p_0/p)^{R/C_p}$, where p_0, p, R, and C_p are surface pressure, pressure, specific gas constant of dry air, and specific heat capacity of dry air, respectively.

2.4 The linear baroclinic model

The LBM developed by Watanabe and Kimoto (2000) is employed in this study. We use a dry version of the LBM which consists of primitive equations linearized about an observed three-dimensional DJF climatology based on ERA5 reanalysis data from 1979 to 2021. The model adopts a T42 horizontal resolution and 20 vertical levels using the sigma coordinate system, and includes horizontal and vertical diffusion, Rayleigh friction, and Newtonian damping. The horizontal diffusion has a damping time scale of 2 h for the smallest wave, and the Rayleigh friction and Newtonian damping have a time scale of $(0.5\ \mathrm{day})^{-1}$ in the lowest three levels and the top level, $(5\ \mathrm{day})^{-1}$ in the fourth level, and $(30\ \mathrm{day})^{-1}$ in the remaining levels. Details of the model formulation are given in Watanabe and Kimoto (2000). To obtain the linear atmospheric response to diabatic forcing, we integrate the model up to 30 days and use averaged results from days 26–30 as the steady response. The circulation response generally approaches a steady state at around day 20.

3 Results

3.1 The PSA modes and SESA rainfall

Figure 1 shows the leading EOF modes of the monthly mean 500 hPa geopotential height anomalies with all seasons pooled together following Mo and Paegle (2001). EOF-1, accounting for approximately 20% of the total variance, exhibits a zonally symmetric pattern with a phase reversal between high- and mid-latitudes (Fig. 1a). EOF-2 and EOF-3, representing the PSA-1 and PSA-2 respectively and accounting for approximately 10% of the total variance, are characterized by a zonally oriented wave train with a zonal wavenumber 3 feature (Fig. 1b–c). However, these two EOF modes cannot be separated according to the North test. Thus, we rotate the EOF modes and obtain REOF modes. The pattern of REOF-1 resembles that of EOF-1 (Fig. 1d). REOF-2 shares similarity with EOF-2, with a dipole pattern over the Pacific and Southern Ocean, but the zonal wave structure and wave center over the Atlantic are not well shown (Fig. 1e). REOF-3 shows a zonally oriented wave train with a zonal wavenumber 3 feature and confines over mid-to-high latitudes, generally within the widely considered PSA sector (the domain within the green lines; Irving and Simmonds 2016) (Fig. 1f). There is a phase shift of approximately 15° of the REOF-3 compared to the PSA-1 and PSA-2.

Given the significant SAMS-related rainfall anomalies over SESA (e.g., Boers et al. 2014; Cherchi et al. 2014; Vera et al. 2018; Díaz et al. 2020) and the increased likelihood of CEPRW occurring over the Atlantic sector (e.g., Li et al. 2015b, 2019) during the austral summer (DJF), our study focuses on this season. Figure 2 shows the interannual variability of the PSA-1, PSA-2, and REOF-3 in austral summer. The correlation between the PSA-1 and

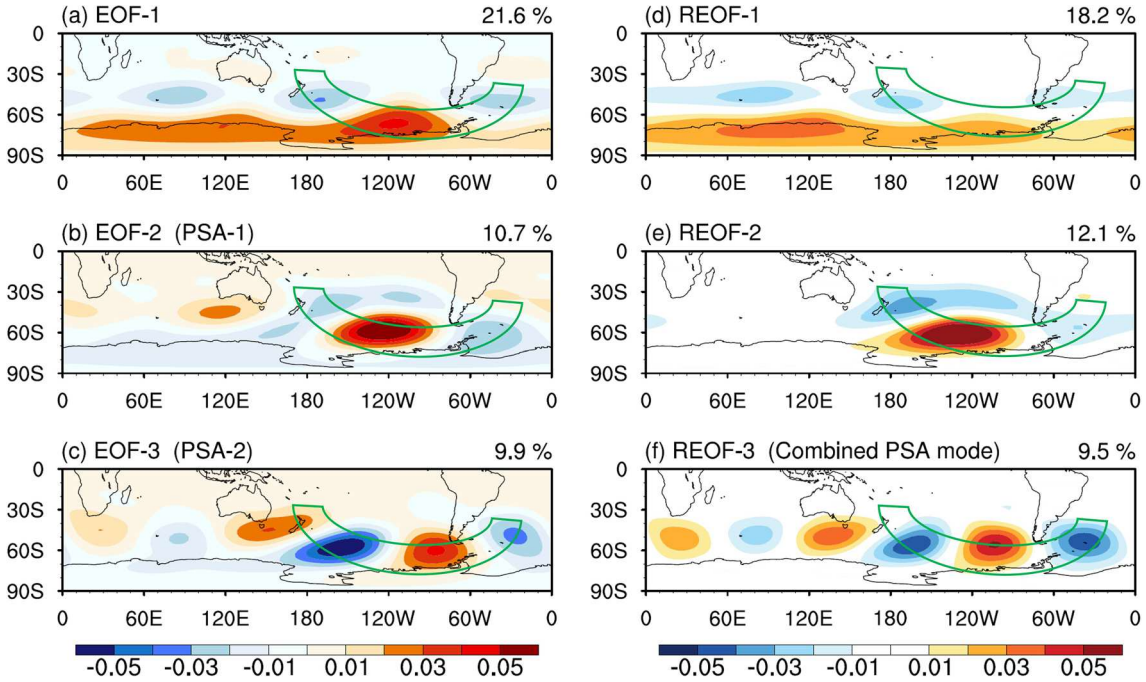

Fig. 1 EOF modes of the monthly mean 500 hPa geopotential height anomalies for **a** EOF-1, **b** EOF-2, and **c** EOF-3. The number shown in the top right corner is the percentage of geopotential height variance explained by the EOF mode. EOF-1 and EOF-2 represent the PSA-1 and PSA-2, respectively. Green lines indicate the widely considered PSA sector. **d–f** Same as **a–c**, but for REOF modes. REOF-3 represents the combined PSA mode, which will be used in this study

REOF-3 is 0.49 and that between the PSA-2 and REOF-3 is 0.70, both significant at 99% confidence level according to the Student's *t*-test. However, the correlation between the PSA-1 and REOF-2 is 0.46 and that between the PSA-2 and REOF-2 is only –0.27, significantly lower than the correlations between REOF-3 and PSA-1/PSA-2. Since REOF-3 pattern is generally within the PSA sector (the domain within the green lines in Fig. 1) and shows high correlations with PSA-1 and PSA-2, REOF-3 is referred to as the combined PSA mode, or simply as the PSA in this study.

On interannual time scales, the PSA is significantly correlated with the Oceanic Niño Index (ONI) at the 95% confidence level, with a correlation coefficient of 0.39. This finding aligns with previous studies (e.g., Karoly 1989; Mo 2000; Mo and Paegle 2001) that suggest the PSA is a response to tropical convection associated with the ENSO. To investigate the relationship between the PSA and South American rainfall on seasonal time scales, we calculate the correlation between the DJF mean PSA index and rainfall anomalies. Figure 3a shows a dipole rainfall structure with positive rainfall anomalies over SESA and negative anomalies to the north, representing the pattern of the South American rainfall dipole identified in previous studies (Nogués-Paegle and Mo 1997; Cherchi et al. 2014; Vera et al. 2018). In addition, the DJF mean PSA is positively correlated with streamfunction anomalies over the southeastern Pacific and northern South America (Fig. 3a).

Due to significant variances in the PSA on intraseasonal time scales (Kiladis and Mo 1998; Mo and Paegle 2001), we identify anomalous events occurring in DJF using the daily index. Following the method in Sect. 2.2, we create the daily PSA index using the daily PC associated with REOF-3 and daily $[\delta Pr]_{\mathrm{SESA}}$ using domain averaged precipitation (within the gray box in Fig. 3a). Figure 3b shows that daily PSA and $[\delta Pr]_{\mathrm{SESA}}$ have no significant correlation during DJF (represented by gray dots), indicating that a strong PSA does not necessarily lead to strong SESA rainfall, nor does strong SESA rainfall lead to a strong PSA. The correlation between the DJF mean PSA index and SESA rainfall anomalies is significant, but it weakens at intraseasonal (daily) time scales. This is primarily because, on daily time scales, SESA rainfall exhibits larger fluctuations, while the PSA shows lower variability with consistent phases lasting from a few days to several weeks (Fig. S1). These large daily fluctuations in SESA rainfall tend to cancel out over a seasonal time scale, leading to a stronger correlation with the PSA. Although the statistical correlation between the two daily indices is insignificant, we will focus on some anomalous events and aim to understand whether strong SESA rainfall produces a different PSA pattern compared to weak SESA rainfall. In this study, we will specifically examine whether strong

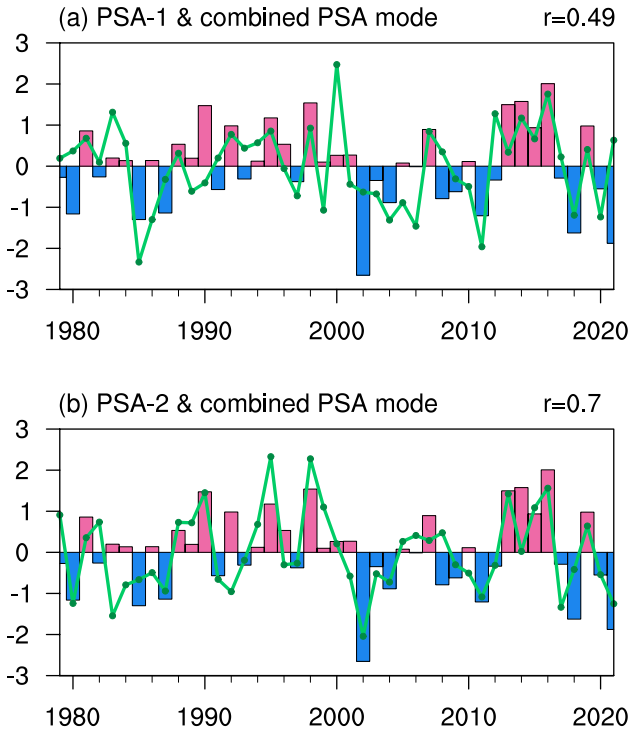

Fig. 2 **a** The detrended PCs averaged in DJF during 1979–2021 for the PSA-1 (green line) and combined PSA mode (i.e., REOF-3; bars), respectively. The number shown in the top right corner is the correlation coefficient between the PSA-1 and combined PSA mode. **b** Same as **a**, but for the PSA-2 (green line)

SESA rainfall can extend the PSA pattern into the Northern Hemisphere.

We focus on daily events where the positive phase of PSA (PSA ≥ 1) coincides with strong SESA rainfall ($[\delta Pr]_{\mathrm{SESA}} \geq 1$) (pink dots in Fig. 3b). A total of 100 anomalous events with daily PSA ≥ 1 and $[\delta Pr]_{\mathrm{SESA}} \geq 1$ can be captured in DJF during 1979–2021. We calculate the duration (i.e., the total number of consecutive days meeting the criterion mentioned above) and 68% of the events are short-lasting events and 8% of the events last 3 days or more. Next, we explore the connection between lower-frequency variability and higher-frequency variability. Figure 3c shows the number (orange bars) of events with daily PSA ≥ 1 and $[\delta Pr]_{\mathrm{SESA}} \geq 1$ in each year. The interannual variability of the number is quite large, ranging from zero to six events per year. We also compute seasonal mean index by averaging the daily index in DJF for each year and then identify anomalous years with DJF mean PSA ≥ 0.5 and $[\delta Pr]_{\mathrm{SESA}} \geq 0.5$. We use 0.5 as threshold to allow more years to be captured. A total of six anomalous years (red triangle markers) are identified, including four years with a relatively large number of anomalous events (1992, 1998, 2007, and 2016). This suggests that the intraseasonal variability indicated by these events is also reflected on interannual time scales.

3.2 Observational evidence of the extension of the PSA by SESA rainfall

In this section, we examine atmospheric circulation patterns associated with the events with strong or weak $[\delta Pr]_{\mathrm{SESA}}$. To understand the role of $[\delta Pr]_{\mathrm{SESA}}$, we identify another group of events without strong $[\delta Pr]_{\mathrm{SESA}}$, defined as daily PSA ≥ 1 and $-0.25 < [\delta Pr]_{\mathrm{SESA}} < 0.25$, and a total of 107 events are identified. We set this threshold to represent weak $[\delta Pr]_{\mathrm{SESA}}$, ensuring a comparable number of events between the strong (100 events) and weak (107 events) groups. To obtain a better representation in the tropics, we will utilize standardized atmospheric circulation patterns as suggested by Bowerman et al. (2017) and Zhao et al. (2023). Figure 4 compares the evolution map of 200 hPa streamfunction and near-surface winds between the PSA events with weak $[\delta Pr]_{\mathrm{SESA}}$ (upper row) and strong $[\delta Pr]_{\mathrm{SESA}}$ (bottom row). Note that the sign of streamfunction anomalies over the Southern Hemisphere is opposite to that of geopotential height anomalies shown in REOF-3 (Fig. 1f). The bootstrap significance test is applied to determine if anomalous fields are significant at the 95% confidence level (Efron and Tibshirani 1994).

For PSA events with weak $[\delta Pr]_{\mathrm{SESA}}$, negative and positive streamfunction anomalies at 60ºS slightly increase in magnitude from Day − 1 to Day + 1 and weaken from Day + 3 to Day + 5 (Fig. 4a–d), but the locations of these anomalous centers change very slowly, indicating the presence of quasi-stationary Rossby waves. This slow-moving structure is consistent with the characteristics of the PSA, which predominantly occurs within an intraseasonal (10–90 day) band (Mo and Paegle 2001). In addition to this zonally oriented wave train at 60ºS, negative streamfunction anomalies appear over SESA from Day −1 (Fig. 4a). The negative streamfunction anomalies over SESA may be triggered by positive streamfunction anomalies associated with the zonal wave train at 60ºS (i.e., the rightmost positive anomalies), suggesting that the PSA has the potential to excite equatorward-propagating circulation anomalies on intraseasonal time scales. However, when $[\delta Pr]_{\mathrm{SESA}}$ is weak, there is no clear evidence that the negative streamfunction anomalies over SESA can further excite cross-equatorial waves or lead to significant growth of circulation anomalies in the tropics. This suggests that the dominant activities of the PSA are confined to the Southern Hemisphere when rainfall anomalies over SESA are weak.

For PSA events with strong $[\delta Pr]_{\mathrm{SESA}}$, a stronger easterly low-level (represented by near-surface winds) flow from the Atlantic turns southward upon reaching the Andes Mountains, bringing more moisture and intensifying $[\delta Pr]_{\mathrm{SESA}}$ (Fig. 4e). The strong rainfall anomalies can act as a source of diabatic heating, generate a Rossby wave train through baroclinic processes (e.g., Danard 1964; Emanuel et al. 1987; Lapeyre and Held 2004; Zhao et al. 2018), and further

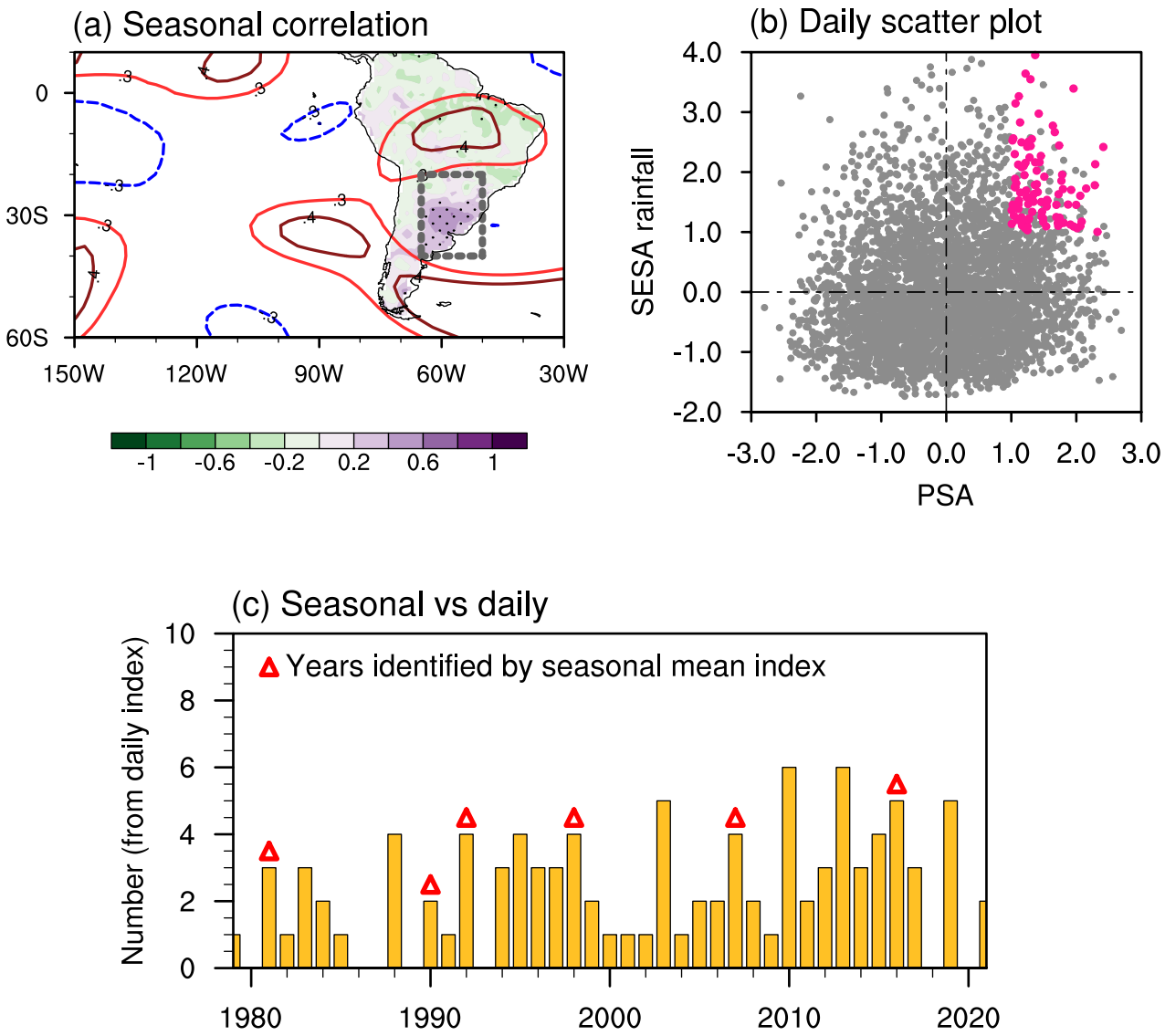

Fig. 3 **a** Correlation coefficients between the detrended PC averaged in DJF for the PSA and DJF mean precipitation (shading) and 200 hPa streamfunction (contours). Stippling indicates precipitation significant at the 95% level according to the Student's *t*-test. The region of SESA is shown within the gray box (20°S–40°S, 50°W–65°W). **b** Scatter plot for the daily PSA index versus daily $[\delta Pr]_{\mathrm{SESA}}$ in DJF (gray dots). The pink dots indicate the events with daily PSA ≥ 1 and $[\delta Pr]_{\mathrm{SESA}} \geq 1$. **c** The total number (orange bars) of events with daily PSA ≥ 1 and $[\delta Pr]_{\mathrm{SESA}} \geq 1$ for each year of 1979–2021 in DJF. The red triangle markers denote the years with seasonal mean (DJF mean) PSA ≥ 0.5 and $[\delta Pr]_{\mathrm{SESA}} \geq 0.5$

amplify the negative streamfunction anomalies over SESA from Day − 1 to Day + 1 (Fig. 4e–f). Compared to PSA events with weak $[\delta Pr]_{\mathrm{SESA}}$ (Fig. 4b), the negative streamfunction anomalies over SESA with strong $[\delta Pr]_{\mathrm{SESA}}$ are larger in magnitudes (Fig. 4f) and provide a more favorable condition for exciting cross-equatorial waves. From Day + 1, the northeastward propagating quasi-stationary wave train becomes clearer, following a great circle path (the magenta curve) in a southwest–northeast direction (Fig. 4f). Circulation anomalies over the tropical Atlantic, southern Europe and northern Africa are amplified and peak in Day + 3 (Fig. 4g), indicating the observational evidence of CEPRW. CEPRW originated from SESA or surrounding region has been identified in previous studies (e.g., Li et al. 2019; Zhao et al. 2023). The northeastward propagating wave train and the zonally oriented wave train at higher latitudes together indicate the cross-equatorial extension of the PSA. The connection between these two wave trains is the negative streamfunction anomalies over SESA, which are significantly amplified by strong SESA rainfall anomalies and extend the PSA further north. On Day + 5, CEPRW weakens as SESA rainfall anomalies decrease (Fig. 4h).

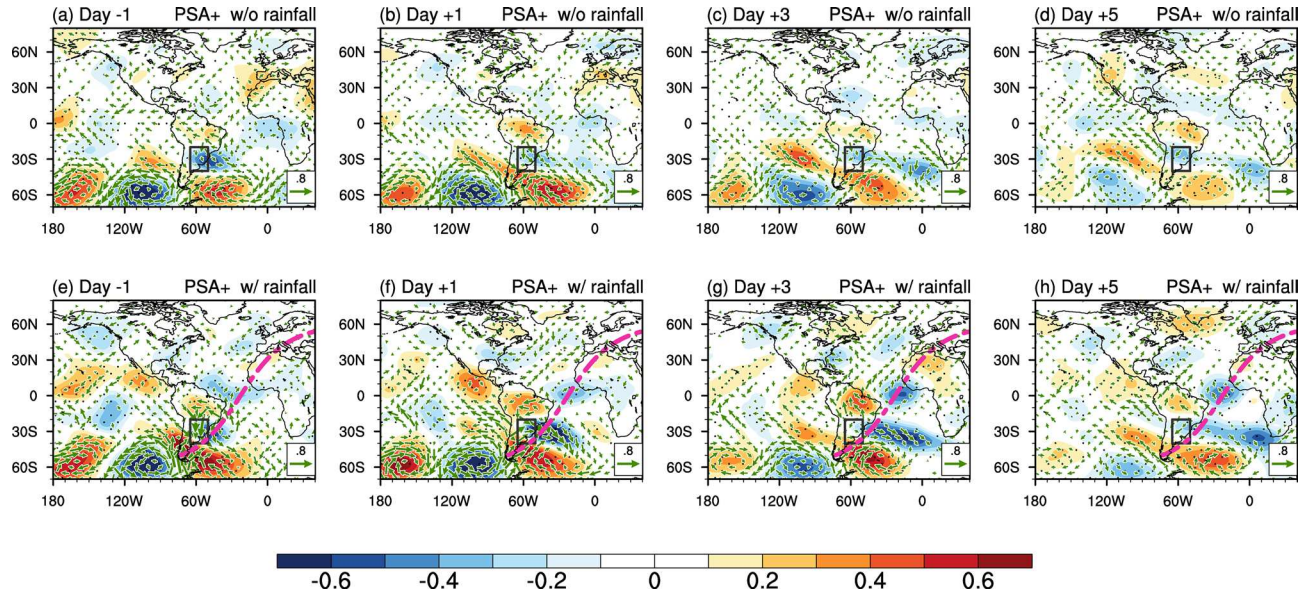

Fig. 4 **a–d** Composite anomalies of standardized 200 hPa streamfunction (shading) and standardized near-surface (10 m) wind (vectors) anomalies from Day –1 to Day + 5 for selected events with daily PSA ≥ 1 and $-0.25 < [\delta Pr]_{\mathrm{SESA}} < 0.25$. Stippling indicates streamfunction significant at the 95% level according to the bootstrap test. Only wind vectors significant at the 95% level are shown. The region of the SESA is shown within the black box (20ºS–40ºS, 50ºW–65ºW). **e–h** Same as **a–d**, but for selected events with daily PSA ≥ 1 and $[\delta Pr]_{\mathrm{SESA}} \geq 1$. The magenta curve indicates the pathway of the cross-equatorial wave train

To further investigate the factors influencing the strength of the cross-equatorial wave train, we conduct a series of observational sensitivity tests. We define a CEPRW index as $\sqrt{sf(30°\mathrm{S}, 40°\mathrm{W})^2 + sf(0°, 20°\mathrm{W})^2 + sf(30°\mathrm{N}, 0°)^2}$, where $sf()$ indicates streamfunction anomalies at each location on the great circle path (the magenta curve in Fig. 4). We first examine how $[\delta Pr]_{\mathrm{SESA}}$ magnitudes influence the CEPRW index. When $[\delta Pr]_{\mathrm{SESA}}$ becomes stronger (Fig. 5b), the PSA index does not necessarily become stronger in

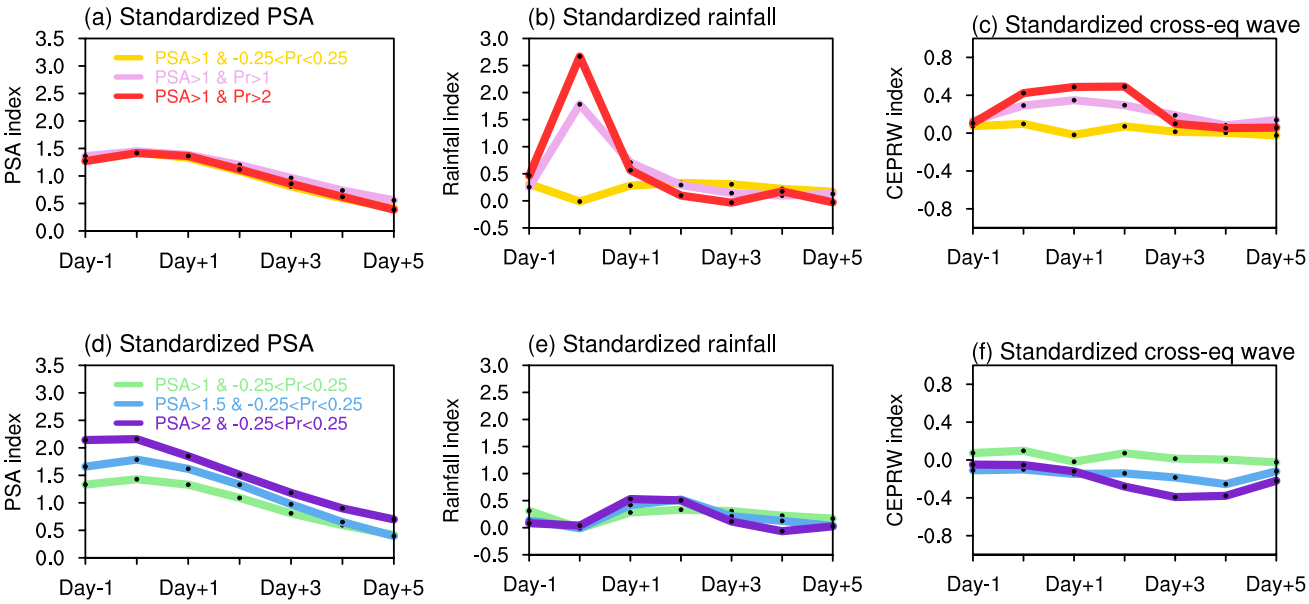

Fig. 5 The evolution of the daily **a** PSA index, **b** $[\delta Pr]_{\mathrm{SESA}}$, and **c** CEPRW index averaged for selected events with daily PSA ≥ 1 and different thresholds of $[\delta Pr]_{\mathrm{SESA}}$ (shown as different colors of lines). **d–f** Same as **a–c**, but for selected events with $-0.25 < [\delta Pr]_{\mathrm{SESA}} < 0.25$ and different thresholds of the PSA index

magnitudes (Fig. 5a), consistent with the insignificant statistical correlation between the PSA and $[\delta Pr]_{SESA}$ (Fig. 3b). The CEPRW index clearly becomes stronger from Day 0 when $[\delta Pr]_{SESA}$ peaks and the influence of stronger $[\delta Pr]_{SESA}$ can last for three days (from Day 0 to Day + 2) (Fig. 5c). Next, we examine how PSA magnitudes influence the CEPRW index. A stronger PSA (Fig. 5d) can only slightly increase $[\delta Pr]_{SESA}$ at Day + 1 (Fig. 5e), but such increase is insignificant at the 95% confidence level according to the bootstrap test, suggesting that the strong $[\delta Pr]_{SESA}$ seen in Fig. 4e–h is not mainly triggered by the PSA but may instead be related to SAMS (e.g., Boers et al. 2014; Cherchi et al. 2014; Vera et al. 2018; Díaz et al. 2020). Figure 5f shows that increasing PSA magnitudes does not lead to a stronger CEPRW index. This suggests that the strength of the CEPRW is primarily driven by the magnitude of SESA rainfall rather than the PSA. The results above provide observational evidence that zonally oriented PSA at higher latitudes can be extended to the tropics and even the Northern Hemisphere when strong rainfall anomalies appear over SESA.

We move a step further to show how cross-equatorial wave influences weather patterns in the Northern Hemisphere. Figure 6 shows the change in precipitation and near-surface temperature over the Eurasia–Africa sector after the peak of SESA rainfall. Before the influence of the CEPRW reaches the extratropical Northern Hemisphere, positive temperature anomalies (red contours) emerge over western and southern Europe, accompanied by positive precipitation anomalies, particularly over the Iberian Peninsula (Fig. 6a). As the influence of the CEPRW intensifies, positive precipitation anomalies propagate eastward across Europe, accompanied by a decrease in surface temperature (Fig. 6b–c). The change of precipitation and surface temperature anomalies is associated with the formation of cyclonic circulations over Europe, as shown by 850 hPa winds. Once the precipitation anomalies move through, surface temperature rises again over western Europe (Fig. 6d). This suggests that the CEPRW can lead to cooler, wetter weather conditions over western and southern Europe.

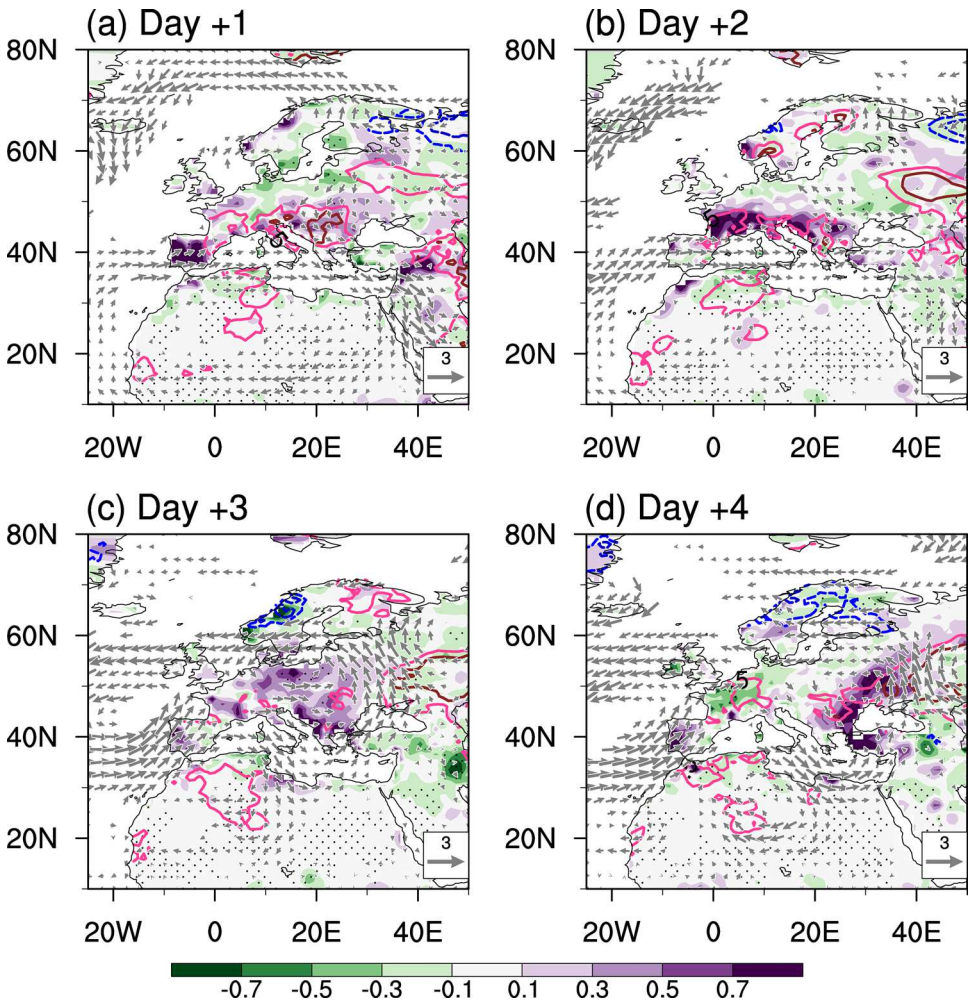

Fig. 6 **a–d** Composite anomalies of precipitation (shading; mm day^{-1}), near-surface temperature (contours; ºC), and 850 hPa winds (vectors; m s^{-1}) from Day + 1 to Day + 4 for selected events with daily PSA ≥ 1 and $[\delta Pr]_{SESA} \geq 1$. Red and blue lines represent the positive (0.5 and 0.8 ºC) and negative (− 0.5 and − 0.8 ºC) values, respectively. Stippling indicates precipitation anomalies significant at the 95% level according to the bootstrap test. Contours and vectors shown are significant at the 95% level

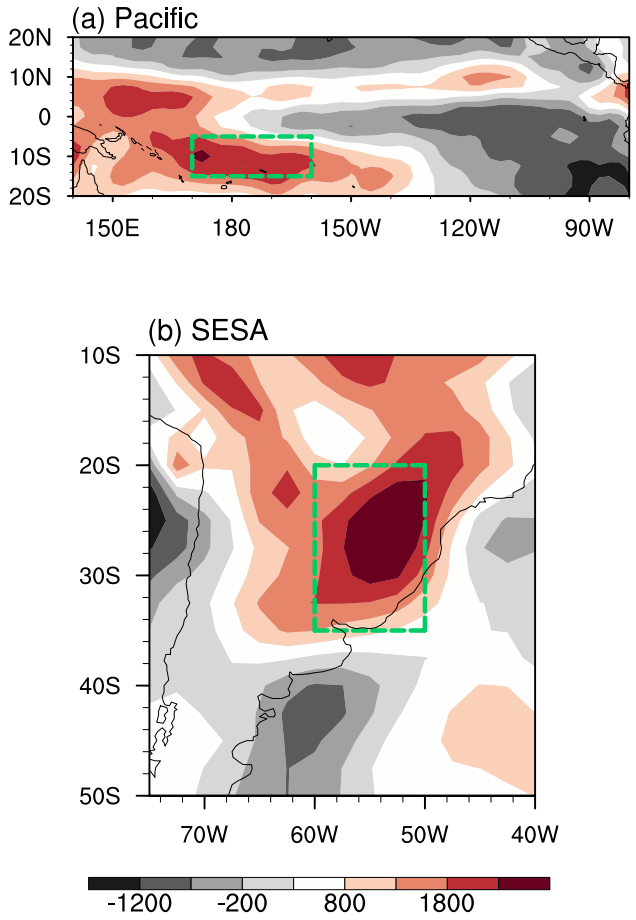

Fig. 7 **a** Composite of 1000–100 hPa vertically integrated Q_1 (K day^{-1}; derived from ERA5) on Day 0 for selected events with daily PSA ≥ 1 over the Pacific. **b** Same as **a**, but for selected events with daily PSA ≥ 1 and $[\delta Pr]_{SESA} \geq 1$ over SESA. The regions of diabatic heating source for the model simulations are shown within the green boxes

3.3 The LBM model simulations

To further explore the role of SESA rainfall, we use the LBM (Watanabe and Kimoto 2000) forced by observed Q_1 over the Pacific and SESA, respectively. Since the PSA is response to tropical convection (e.g., Karoly 1989; Mo 2000; Mo and Paegle 2001), we examine Q_1 for the events on Day 0 with daily PSA ≥ 1. Figure 7a shows the composite of 1000–100 hPa vertically integrated Q_1 for the PSA events (i.e., PSA ≥ 1) over the Pacific derived from ERA5 reanalysis data, revealing that the largest Q_1 value appears over the central Pacific in the Southern Hemisphere. Figure 7b shows the same field for the PSA events with strong $[\delta Pr]_{SESA}$ (i.e., PSA ≥ 1 and $[\delta Pr]_{SESA} \geq 1$) over South America. As expected, the largest Q_1 value appears over SESA. Sensitivity tests suggest that very similar results are obtained when using the composite Q_1 for the strong $[\delta Pr]_{SESA}$ events without constraint of the PSA.

Next, we average Q_1 over the selected domain over the Pacific and SESA (within the green boxes in Fig. 7), respectively. The vertical profiles of Q_1 for the two domains share some similarities, showing an increase from the surface to 400 hPa, followed by a decrease toward the upper troposphere (Fig. 8). The difference between the two profiles is that Q_1 at 400 hPa over SESA is larger, attributable to the convective activity associated with strong rainfall anomalies in this region. The heating source of the two domains is obtained by multiplying the observed Q_1 pattern (within the green box of Fig. 7) by associated vertical profile for each domain (Fig. 8). Since we focus on the heating source, the negative values of Q_1 are excluded.

Using heating source over the Pacific, we run the LBM following the method in Sect. 2.4. The Pacific heating source (indicated by the green contour) induces 200 hPa

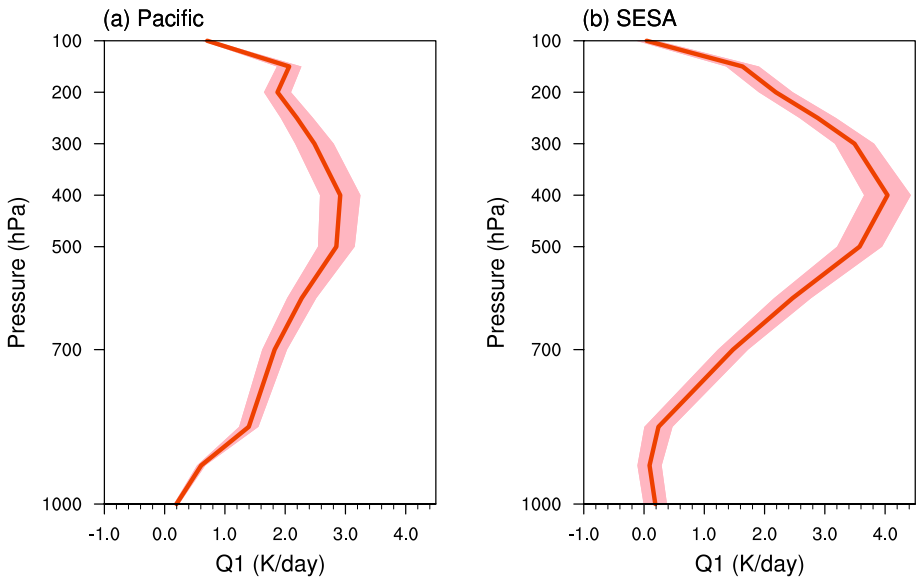

Fig. 8 **a** The mean Q_1 (K day^{-1}; derived from ERA5; thick red curve) from 1000 to 100 hPa averaged for the selected events (Day 0) with daily PSA ≥ 1 averaged in the green box (15°S–5°S, 170°E–160°W) of Fig. 7a. Shading represents the spread of the minimum and maximum values of the domain averaged Q_1 among selected events. **b** Same as **a**, but for selected events with daily PSA ≥ 1 and $[\delta Pr]_{SESA} \geq 1$ averaged in the green box (35°S–20°S, 60°W–50°W) of Fig. 7b

streamfunction anomalies with negative anomalies to the west and positive anomalies to the east over the southern hemispheric Pacific (Fig. 9a). The model successfully simulates the positive anomalies to the west of South America, aligning well with the observed streamfunction anomalies in Fig. 3a. However, the observed negative anomalies over high latitudes around 60ºS are simulated further west and with smaller magnitudes. The discrepancies between the observed and simulated PSA patterns may be due to the idealized experiment design, which prescribes only the tropical heating source over the selected area. Over the Atlantic sector, a series of streamfunction anomalies can be seen, though they may not represent the PSA extending from the Pacific.

When incorporating the heating source over SESA (indicated by the green contour) into the model, a Rossby wave train emerges, extending from the central Pacific via southern South America towards the Atlantic and Africa along a great circle path (shown by the magenta curve) in Fig. 9b. This wave train pattern bears some similarities to the observed pattern in Fig. 4f, particularly over the Atlantic sector, suggesting a possible northeastward extension of the PSA due to SESA rainfall forcing. The circulation pattern resulting from both Pacific and SESA forcings reflects a linear combination of the Pacific forcing and SESA forcing responses. Moreover, streamfunction anomalies along this wave train path are intensified and extended compared to the experiment with only the Pacific heating source prescribed, as seen in the positive anomalies over the South Pacific near 50ºS, 90ºW and those over the Atlantic and African sector (Fig. 9b vs 9a). Sensitivity tests have been conducted, including selecting a larger domain for the forcing, but the results remain largely consistent with those shown in Fig. 9. The LBM experiments corroborate the observational evidence, demonstrating that rainfall anomalies over SESA can extend the PSA to the Northern Hemisphere.

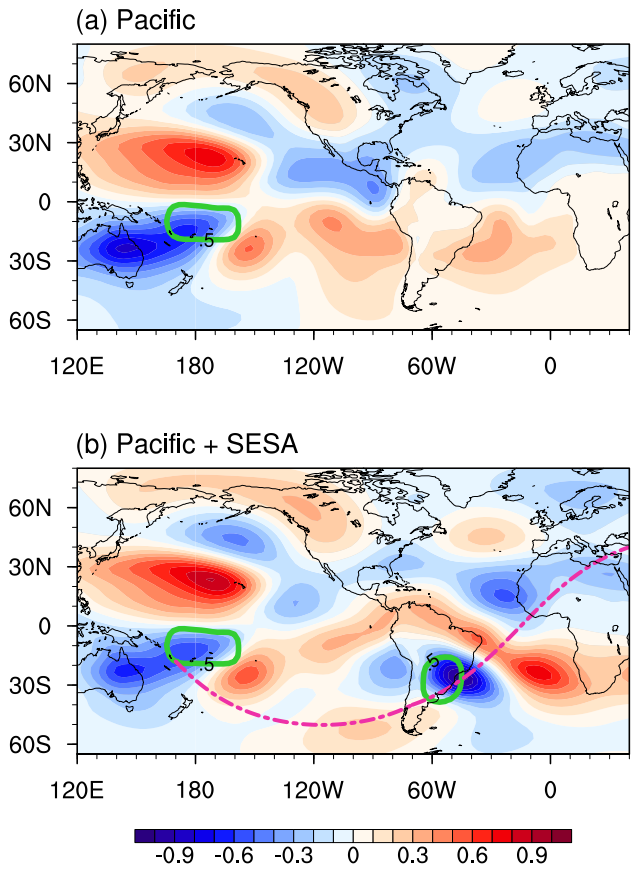

Fig. 9 **a** The steady state of the LBM simulation of the 200 hPa streamfunction anomalies (shading; $m^2\ s^{-1}$; zonal mean removed) response to the observed heating over the Pacific. The contour denotes the prescribed $Q_1 \geq 0.5$ K day^{-1} at 400 hPa derived from the observation. **b** Same as **a**, but for the response to the observed heating over both the Pacific and SESA. The magenta curve in **b** indicates the pathway of the wave train

4 Summary and discussion

This study examines the impact of SESA rainfall anomalies on the PSA during the austral summer. The PSA is identified as REOF-3, characterized by a zonal wavenumber 3 feature, with centers of significant magnitude extending from the central Pacific, across the Southern Ocean, and towards the Atlantic—encompassing the widely recognized PSA sector. REOF-3 better represents both PSA-1 and PSA-2 modes compared to REOF-2. Daily index of the PSA is created based on REOF-3. Following Zhao et al. (2023), we focus on rainfall anomalies over SESA and develop a daily rainfall index, denoted as $[\delta Pr]_{\mathrm{SESA}}$. A total of 100 events for the positive phase of PSA associated with strong $[\delta Pr]_{\mathrm{SESA}}$ are identified in DJF during 1979–2021. The intraseasonal variability indicated by these events is also reflected on interannual time scales, indicated by anomalous years with positive PSA phase and strong $[\delta Pr]_{\mathrm{SESA}}$. When rainfall anomalies over SESA are weak, the dominant activities of the PSA are confined to higher latitudes of the Southern Hemisphere, with no clear evidence of the CEPRW. However, when strong $[\delta Pr]_{\mathrm{SESA}}$ is present, a quasi-stationary Rossby wave train can be generated from the higher latitudes where the PSA is most significant. This wave train propagates downstream along a southwest–northeast great circle path and crosses the equator, representing a cross-equatorial extension of the PSA. As $[\delta Pr]_{\mathrm{SESA}}$ reaches its peak, atmospheric circulation anomalies along this path intensify, inducing a wet and cool weather condition over western and southern Europe. Additional analyses show that the strength of the CEPRW is primarily driven by the magnitude of SESA rainfall rather than the PSA.

To further investigate the influence of $[\delta Pr]_{\mathrm{SESA}}$, we prescribed the observed heat source (Q_1) associated with the PSA alone and with both the PSA and $[\delta Pr]_{\mathrm{SESA}}$ in the

LBM. When incorporating the heat source over SESA into the model, atmospheric circulation anomalies triggered by the central Pacific forcing are extended and amplified, forming a wave train along a great circle path from the central Pacific to northern Africa. The LBM simulations confirm the significant role of $[\delta Pr]_{\mathrm{SESA}}$ in extending the PSA. In this study, we use the dry version of the LBM, which excludes both moisture and eddy feedback. While moisture feedback may amplify the wave response in certain regions and eddy feedback in the mid-latitudes may also have an impact, these factors are secondary in importance compared to the core dynamics of the LBM.

The main conclusions of this study are: (1) the PSA and SESA rainfall are two independent variables, and strong SESA rainfall does not amplify the magnitudes of the PSA index or vice versa; (2) SESA rainfall is the main cause for the CEPRW; and (3) such CEPRW can be regarded as the equatorward extension of the PSA pattern (though the magnitude of the PSA index is unaffected) because negative streamfunction anomalies over SESA connect the zonally oriented wave train (explained by the PSA index) and northeastward propagating wave train (explained by the CEPRW index). It is worth noting that our conclusion—that SESA rainfall can extend the PSA pattern—is not limited to the specific pattern of REOF-3. Similar analyses conducted for PSA-1, PSA-2, and REOF-2 yield comparable results (not shown). Therefore, we expect that applying other methods to identify the PSA pattern would lead to similar conclusions.

This study builds upon the findings of Zhao et al. (2023), further exploring the influence of rainfall variability over SESA on adjacent oceans and continents. To our knowledge, the influence of South American rainfall on adjacent oceans, such as the tropical Atlantic, has not been widely studied. Most previous research has focused on the ocean-to-land direction (e.g., Yoon and Zeng 2010), while the reverse—land-to-ocean—has been largely overlooked. The cross-equatorial pathway of Rossby waves over the Atlantic sector has been identified in earlier studies through numerical model simulations (e.g., Ambrizzi and Hoskins 1997) or diagnostic tools like wave ray tracing (e.g., Li et al. 2019). However, only Zhao et al. (2023) and the present study have linked the CEPRW to South American rainfall and explored the potential impact of SESA rainfall on Northern Hemisphere weather patterns, including Europe. Compared to Zhao et al. (2023), this study takes a further step by connecting SESA rainfall with a well-known atmospheric mode, the PSA.

Our results underscore the crucial role of the South American continent as a land bridge, linking the Pacific and Atlantic Oceans and connecting the Southern and Northern Hemispheres. The knowledge of this study will enhance our understanding of teleconnections between the two ocean basins and interhemispheric relationships through hydroclimate variability over South America. Moreover, this study provides valuable insights for evaluating the likelihood of temperature and precipitation extremes over Europe based on upstream precursory circulation anomalies, as well as for introducing initial condition perturbations in ensemble predictions (e.g., Mariotti et al. 2020). For example, strong PSA events linked to strong SESA rainfall can alert official forecast centers to potential weather extremes in Europe, ultimately enhancing the accuracy of weather extremes predictions on subseasonal time scales.

Supplementary Information The online version contains supplementary material available at https://doi.org/10.1007/s00382-024-07496-5.

Acknowledgements We thank the two anonymous reviewers for their insightful comments. Siyu Z. and R.F. are supported by the U.S. National Science Foundation (Award Number AGS-1917781 and AGS-2404970). Sen Z. and F.F.J. are supported by the U.S. National Science Foundation (Award Number AGS-2219257) and NOAA's Climate Program Office's Modelling, Analysis, Predictions, and Projections (MAPP) Program (Award Number NA23OAR2007440).

Author contributions SZ designed and conducted observational analyses and prepared the manuscript. RF designed the concepts and analyses of the manuscript. SZ and FFJ designed and conducted LBM model simulations. HW provided a basis for an early version of the manuscript. All the authors revised the manuscript and provided helpful comments.

Data availability All the data used in this study are freely available online. The daily precipitation data is from NOAA CPC (https://psl.noaa.gov/data/gridded/data.cpc.globalprecip.html). The ERA5 reanalysis data is from https://doi.org/https://doi.org/10.24381/cds.6860a573. The ONI index is from https://psl.noaa.gov/data/correlation/oni.data.

Code availability The scripts of this study has been uploaded to Zenodo (https://doi.org/https://doi.org/10.5281/zenodo.13751015). For additional questions, please contact the corresponding author at siyu_zhao@atmos.ucla.edu.

Declarations

Conflict of interest The authors have no conflict of interest.

References

Ambrizzi T, Hoskins BJ (1997) Stationary Rossby-wave propagation in a baroclinic atmosphere. Q J R Meteorol Soc 123(540):919–928. https://doi.org/10.1256/smsqj.54006

Boers N, Rheinwalt A, Bookhagen B, Barbosa HMJ, Marwan N, Marengo J, Kurths J (2014) The south American rainfall dipole: a complex network analysis of extreme events. Geophys Res Lett 41(20):7397–7405. https://doi.org/10.1002/2014GL061829

Bowerman A et al (2017) An influence of extreme southern hemisphere cold surges on the North Atlantic Subtropical High through a shallow atmospheric circulation. J Geophys Res 122(10):135–148. https://doi.org/10.1002/2017JD026697

Cai W, McPhaden MJ, Grimm AM et al (2020) Climate impacts of the El Niño-Southern Oscillation on South America. Nat Rev Earth Environ 1:215–231. https://doi.org/10.1038/s43017-020-0040-3

Campitelli E, Díaz LB, Vera C (2023) Revisiting the zonally asymmetric extratropical circulation of the Southern Hemisphere spring using complex empirical orthogonal functions. Clim Dyn 61:3989–4009. https://doi.org/10.1007/s00382-023-06780-0

Chen M, Shi W, Pingping X et al (2008) Assessing objective techniques for gauge-based analyses of global daily precipitation. J Geophys Res 113:D04110. https://doi.org/10.1029/2007JD009132

Cherchi A, Carril AF, Menéndez CG et al (2014) La Plata basin precipitation variability in spring: role of remote SST forcing as simulated by GCM experiments. Clim Dyn 42:219–236. https://doi.org/10.1007/s00382-013-1768-y

Danard MB (1964) On the influence of released latent heat on cyclone development. J Appl Meteorol 3:27–37. https://doi.org/10.1175/1520-0450(1964)0032.0.CO;2

Díaz N, Barreiro M, Rubido N (2020) Intraseasonal predictions for the South American rainfall dipole. Geophys Res Lett 47:e2020GL089985. https://doi.org/10.1029/2020GL089985

Dickinson RE (1968) Planetary Rossby waves propagating vertically through weak westerly wind wave guides. J Atmos Sci 25:984–1002. https://doi.org/10.1175/1520-0469(1968)025%3c0984:PRWPVT%3e2.0.CO;2

Edmon HR, Hoskins BJ, McIntyre ME (1980) Eliassen-Palm cross sections for the troposphere. J Atmos Sci 37(12):2600–2616. https://doi.org/10.1175/1520-0469(1980)037%3c2600:EPCSFT%3e2.0.CO;2

Efron B, Tibshirani RJ (1994) An Introduction to the Bootstrap. Chapman & Hall/CRC Press, Boca Raton, Florida, pp220–223. https://www.routledge.com/An-Introduction-to-the-Bootstrap/Efron-Tibshirani/p/book/9780412042317

Emanuel KA, Fantini M, Thorpe AJ (1987) Baroclinic instability in an environment of small stability to slantwise moist convection. Part I: two-dimensional models. J Atmos Sci 44:1559–1573. https://doi.org/10.1175/1520-0469(1987)0442.0.CO;2

Gelbrecht M, Boers N, Kurths J (2018) Phase coherence between precipitation in South America and Rossby waves. Sci Adv 4:1–9. https://doi.org/10.1126/sciadv.aau3191

Gong T, Feldstein SB, Lee S (2020) Rossby wave propagation from the Arctic into the midlatitudes: Does it arise from in situ latent heating or a trans-Arctic wave train? J Clim 33:3619–3633. https://doi.org/10.1175/JCLI-D-18-0780.1

Goyal R, Jucker M, Gupta AS, England MH (2022) A new zonal wave-3 index for the Southern hemisphere. J Clim 35(15):5137–5149. https://doi.org/10.1175/JCLI-D-21-0927.1

Hayashi M, Watanabe M (2017) ENSO complexity induced by state dependence of westerly wind events. J Clim 30:3401–3420. https://doi.org/10.1175/JCLI-D-16-0406.1

Hersbach H, Bell B, Berrisford P et al (2020) The ERA5 global reanalysis. Q J R Meteorol Soc 146:1999–2049. https://doi.org/10.1002/qj.3803

Hirata FE, Grimm AM (2016) The role of synoptic and intraseasonal anomalies in the life cycle of summer rainfall extremes over South America. Clim Dyn. https://doi.org/10.1007/s00382-015-2751-6

Hoskins BJ, Ambrizzi T (1993) Rossby wave propagation on a realistic longitudinally varying flow. J Atmos Sci 50:1661–1671. https://doi.org/10.1175/1520-0469(1993)0502.0.CO;2

Hoskins B, Karoly D (1981) The steady linear response of a spherical atmosphere to thermal and orographic forcing. J Atmos Sci 38:1179–1196. https://doi.org/10.1175/1520-0469(1981)0382.0.CO;2

Hsu HH, Lin SH (1992) Global teleconnections in the 250-mb streamfunction field during the Northern Hemisphere winter. Mon Weather Rev 120(7):1169–1190. https://doi.org/10.1175/1520-0493(1992)1202.0.CO;2

Irving D, Simmonds I (2016) A new method for identifying the Pacific-South American Pattern and its influence on regional climate variability. J Clim 29(17):6109–6125. https://doi.org/10.1175/JCLI-D-15-0843.1

Junquas C, Li L, Vera CS, Le Treut H, Takahashi K (2016) Influence of South America orography on summertime precipitation in Southeastern South America. Clim Dyn 46:3941–3963. https://doi.org/10.1007/s00382-015-2814-8

Karoly DJ (1989) Southern hemisphere circulation features associated with El Niño-Southern Oscillation events. J Clim 2(11):1239–1252. https://doi.org/10.1175/1520-0442(1989)002h1239:SHCFAWi2.0.CO;2

Kiladis GN, Mo KC (1998) Interannual and intraseasonal variability in the Southern Hemisphere. In: Karoly DJ, Vincent DG (eds) Meteorology of the Southern Hemisphere. Am Meteorol Soc, Boston, pp 307–336

Kousky VE, Kagano MT, Cavalcanti IFA (1984) A review of the Southern Oscillation: oceanic-atmospheric circulation changes and related rainfall anomalies. Tellus Dyn Meteorol Oceanogr 36:490–504. https://doi.org/10.1111/j.1600-0870.1984.tb00264.x

Lapeyre G, Held IM (2004) The role of moisture in the dynamics and energetics of turbulent baroclinic eddies. J Atmos Sci 61(14):1693–1710. https://doi.org/10.1175/1520-0469(2004)0612.0.CO;2

Li X, Holland DM, Gerber EP et al (2015a) Rossby waves mediate impacts of tropical oceans on West Antarctic atmospheric circulation in austral winter. J Clim 28(20):8151–8164. https://doi.org/10.1175/JCLI-D-15-0113.1

Li Y, Li J, Jin FF, Zhao S (2015b) Interhemispheric propagation of stationary Rossby waves in a horizontally nonuniform background flow. J Atmos Sci 72(8):3233–3256. https://doi.org/10.1175/JAS-D-14-0239.1

Li YJ, Feng J, Li JP, Hu AX (2019) Equatorial windows and barriers for stationary Rossby wave propagation. J Clim 32:6117–6135. https://doi.org/10.1175/JCLI-D-18-0722.1

Ling J, Zhang C (2013) Diabatic heating profiles in recent global reanalyses. J Clim 26:3307–3325. https://doi.org/10.1175/JCLI-D-12-00384.1

Lou J, O'Kane TJ, Holbrook NJ (2021) Linking the atmospheric Pacific-South American mode with oceanic variability and predictability. Commun Earth Environ 2:223. https://doi.org/10.1038/s43247-021-00295-4

Mariotti A et al (2020) Windows of opportunity for skillful forecasts subseasonal to seasonal and beyond. Bull Amer Met Soc 101(5):E608–E625. https://doi.org/10.1175/BAMS-D-18-0326.1

Mo KC (2000) Relationships between low-frequency variability in the Southern Hemisphere and sea surface temperature anomalies. J

Clim 13:3599–3610. https://doi.org/10.1175/1520-0442(2000)0132.0.CO;2
Mo KC, Higgins RW (1998) The Pacific-South American modes and tropical convection during the Southern Hemisphere Winter. Mon Wea Rev 126:1581–1596. https://doi.org/10.1175/1520-0493(1998)1262.0.CO;2
Mo KC, Paegle JN (2001) The Pacific-South American modes and their downstream effects. Int J Climatol 21:1211–1229. https://doi.org/10.1002/joc.685
Müller GV, Ambrizzi T (2007) Teleconnection patterns and Rossby wave propagation associated to generalized frosts over southern South America. Clim Dyn 29:633–645. https://doi.org/10.1007/s00382-007-0253-x
Nogués-Paegle J, Mo KC (1997) Alternating wet and dry conditions over South America during summer. Mon Weather Rev 125(2):279–291. https://doi.org/10.1175/1520-0493(1997)125
North GR, Bell TL, Cahalan RF, Moeng FJ (1982) Sampling errors in the estimation of empirical orthogonal functions. Mon Weather Rev 110:699–706. https://doi.org/10.1175/1520-0493(1982)110%3c0699:SEITEO%3e2.0.CO;2
Reboita MS, Ambrizzi T, Crespo NM, Dutra LM, Ferreira GW, Rehbein A, Drumond A, da Rocha RP, Souza CA (2021) Impacts of teleconnection patterns on South America climate. Ann New York Acad Sci 1504(1):116–153. https://doi.org/10.1111/nyas.14592
Renwick JA, Revell MJ (1999) Blocking over the South Pacific and Rossby wave propagation. Mon Weather Rev 127:2233–2247. https://doi.org/10.1175/1520-0493(1999)1272.0.CO;2
Richman MB (1986) Rotation of Principal Components J Climatol 3:293–335. https://doi.org/10.1002/joc.3370060305
Risbey JS, Monselesan DP et al (2021) The identification of long-lived southern hemisphere flow events using archetypes and principal components. Mon Weather Rev 149(6):1987–2010. https://doi.org/10.1175/MWR-D-20-0314.1
Schneider EK, Watterson IG (1984) Stationary Rossby wave propagation through easterly layers. J Atmos Sci 41:2069–2083. https://doi.org/10.1175/1520-0469(1984)041%3c2069:srwpte%3e2.0.co;2
Thomas RA, Webster PJ (1994) Horizontal and vertical structure of cross-equatorial wave propagation. J Atmos Sci 51:1417–1430. https://doi.org/10.1175/1520-0469(1994)0512.0.CO;2
Ting M (1996) Steady linear response to tropical heating in barotropic and baroclinic models. J Atmos Sci 53:1698–1709. https://doi.org/10.1175/1520-0469(1996)053%3c1698:SLRTTH%3e2.0.CO;2
Tseng KC, Maloney E, Barnes EA (2019) The consistency of MJO teleconnection patterns: an explanation using linear Rossby wave theory. J Clim 32:531–548. https://doi.org/10.1175/JCLI-D-18-0211.1
Tseng KC, Maloney E, Barnes EA (2020) The consistency of MJO teleconnection patterns on interannual time scales. J Clim 33:3471–3486. https://doi.org/10.1175/JCLI-D-19-0510.1
Vera CS, Alvarez MS, Gonzalez PLM, Liebmann B, Kiladis GN (2018) Seasonal cycle of precipitation variability in South America on intraseasonal timescales. Clim Dyn 51(5):1991–2001. https://doi.org/10.1007/s00382-017-3994-1
Wang C (2019) Three-ocean interactions and climate variability: a review and perspective. Clim Dyn 53:18. https://doi.org/10.1007/s00382-019-04930-x
Watanabe M, Kimoto M (2000) Atmosphere-ocean thermal coupling in the North Atlantic: a positive feedback. Q J R Meteorol Soc 26:3343–3369. https://doi.org/10.1002/qj.49712657017
Webster PJ, Holton JR (1982) Cross-equatorial response to middle-latitude forcing in a zonally varying basic state. J Atmos Sci 39(4):722–733. https://doi.org/10.1175/1520-0469(1982)0392.0.CO;2
Yanai M, Esbensen S, Chu J-H (1973) Determination of bulk properties of tropical cloud clusters from large-scale heat and moisture budgets. J Atmos Sci 30:611–627. https://doi.org/10.1175/1520-0469(1973)0302.0.CO;2
Yang S, Webster PJ (1990) The Effect of summer tropical heating on the location and intensity of the extratropical westerly jet streams. J Geophys Res 95:18705. https://doi.org/10.1029/JD095iD11p18705
Yasui S, Watanabe M (2010) Forcing processes of the summertime circumglobal teleconnection pattern in a dry AGCM. J Climate 23:2093–2114. https://doi.org/10.1175/2009JCLI3323.1
Yoon JH, Zeng N (2010) An Atlantic influence on Amazon rainfall. Clim Dyn. https://doi.org/10.1007/s00382-009-0551-6
Zermeno-Diaz D, Zhang C (2013) Possible root causes of surface westerly biases over the equatorial Atlantic in global climate models. J Clim 26:8154–8168. https://doi.org/10.1175/JCLI-D-12-00226.1
Zhao S, Li JP, Li Y (2015) Dynamics of an Interhemispheric Teleconnection across the Critical Latitude through a Southerly Duct during Boreal Winter. J Climate 28:7437–7456. https://doi.org/10.1175/JCLI-D-14-00425.1
Zhao S, Deng Y, Black RX (2018) An intraseasonal mode of atmospheric variability relevant to the U.S. hydroclimate in boreal summer: dynamic origin and East Asia connection. J Clim 31:9855–9868. https://doi.org/10.1175/JCLI-D-18-0206.1
Zhao S, Li JP, Li Y, Jin F-F, Zheng J (2019) Interhemispheric influence of Indo-Pacific convection oscillation on Southern Hemisphere rainfall through southward propagation of Rossby waves. Clim Dyn 52:3203–3221. https://doi.org/10.1007/s00382-018-4324-y
Zhao S, Fu R, Wang H, Jin F-F (2023) The influence of southeastern South American rainfall on weather patterns over the tropical Atlantic, northwestern Africa and western Europe. J Geophys Res Atmos 128:e2023JD039447. https://doi.org/10.1029/2023JD039447